Feasibility of electromagnetic methods to detect and image steam-assisted gravity drainage steam chambers

Sarah G. R. Devriese[1] and Douglas W. Oldenburg[1]

ABSTRACT

We have investigated the use of electric and electromagnetic (EM) methods to monitor the growth of steam-assisted gravity drainage (SAGD) steam chambers. SAGD has proven to be a successful method for extracting bitumen from the Athabasca oil sands in Alberta, Canada. However, complexity and heterogeneity within the reservoir could impede steam chamber growth, thereby limiting oil recovery and increase production costs. Using seismic data collected over an existing SAGD project, we have generated a synthetic steam chamber and modeled it as a conductive body within the bitumen-rich McMurray Formation. Simulated data from standard crosswell electrical surveys, when inverted in three dimensions, show existence of the chamber but lack the resolution necessary to determine the shape and size. By expanding to EM surveys, our ability to recover and resolve the steam chamber is significantly enhanced. We use a simplified survey design procedure to design a variety of field surveys that include surface and borehole transmitters operating in the frequency or time domain. Each survey is inverted in three dimensions, and the results are compared. Importantly, despite the shielding effects of the highly conductive cap rock over the McMurray Formation, we have determined that it is possible to electromagnetically excite the steam chamber using a large-loop surface transmitter. This motivates a synthetic example, constructed using the geology and resistivity logging data of a future SAGD site, where we simulate data from single and multiple surface loop transmitters. We have found that even when measurements are restricted to the vertical component of the electric field in standard observation wells, if multiple transmitters are used, the inversion recovers three steam chambers and discerns an area of limited steam growth that results from a blockage in the reservoir. The effectiveness of the survey shows that this EM methodology is worthy of future investigation and field deployment.

INTRODUCTION

Steam-assisted gravity drainage (SAGD) is an in situ recovery process used to extract bitumen from the Athabasca oil sands in Northern Alberta. It uses two horizontal wells drilled at the bottom of the reservoir (Dembicki, 2001), where steam is injected into the top well and produces a steam chamber that grows upward and outward. The heated fluid oil and condensed water at the edge of the chamber flow through the formation and are collected by the producing well. As the oil drains, the chamber expands farther into the bitumen reservoir (Butler, 1994). Al-Bahlani and Babadagli (2009) provide a detailed history of SAGD development.

The success of this technique depends on being able to propagate steam throughout the reservoir, but heterogeneity can prevent this (Zhang et al., 2007; Strobl et al., 2013). Instead of the idealized balloon shape (Figure 1a), the steam chamber may develop irregularly (Figure 1b). This affects the amount of oil that can be produced and illustrates the need to monitor the growth of SAGD steam chambers. Successful monitoring can help optimize production efforts by further understanding the reservoir, decreasing the steam-to-oil ratio (i.e., the amount of water needed to produce a unit of oil), locating missed pay, identifying thief zones (i.e., steam that escapes via unexpected paths such as faults), and more efficiently using resources (Singhai and Card, 1988).

Currently, seismic imaging methods are the predominant monitoring procedures (e.g., Forgues et al., 2006; Wolf et al., 2008). Although often successful, seismic data can be expensive to collect and time-consuming to process (Engelmark, 2007). Other methods to monitor steam flooding include temperature measurements (Krawchuk et al., 2006), pressure logging, and resistivity logging (Ranganayaki et al., 1992). Gravity has been used for waterflood monitoring in a reservoir (Ferguson et al., 2008) and investigated for SAGD use by Reitz et al. (2015). Electrical and electromagnetic (EM) methods have a large presence in fluid monitoring (e.g., LaBrecque et al., 1996; Oldenborger et al., 2007). The injection of steam into an oil reservoir alters its resistivity (Butler and Knight, 1998), and hence, electrical resistivity tomography (ERT) and crosswell electromagnetics have been used to monitor steam growth (Ramirez et al., 1993; Marion et al., 2011). ERT has also shown success in delineating normal-shaped steam chambers due to SAGD in two dimensions (Tøndel et al., 2014). However, SAGD steam chambers are 3D structures that may grow irregularly, and thus they need to be monitored in three dimensions. In addition, electric and EM surveys can be collected more frequently than seismic data, especially when using permanent installations, such as Tøndel et al. (2014). Thus, EM methods have great potential to image SAGD steam chambers, but these methodologies have not been rigorously tested (Engelmark, 2010).

The motivation of this paper is twofold. First, we identify the feasibility of using electric and EM methods for detecting and imaging a small, irregular steam chamber. We investigate common transmitter and receiver types for the DC component, as well as frequency- and time-domain EM. Second, we present a synthetic example based on a field site in the Athabasca oil sands. The model has three SAGD chambers, and the middle chamber has a blockage.

To explore cost-effective strategies, we focus upon the use of large-scale inductive transmitters on the surface with acquisition of data in observational wells that mimic those for current SAGD operations. We show that the blockage can be imaged with a single transmitter and readily acquired electrical potentials in the wells. The image resolution is improved with an additional transmitter, and this highlights the importance of survey design and exciting the target from multiple directions. We conclude the paper with a discussion on the merits of using EM for SAGD monitoring.

BACKGROUND

Electromagnetics

EM methods are geophysical exploration tools used to find contrasts in electrical resistivity. The underlying equations are Maxwell's, which, assuming the quasistatic approximation, are written in the time domain as

$$\nabla \times \mathbf{e} + \frac{\partial \mathbf{b}}{\partial t} = 0, \tag{1}$$

$$\nabla \times \mathbf{h} - \sigma \mathbf{e} = \mathbf{j}_e. \tag{2}$$

In equations 1 and 2, $\mathbf{e}$ is the electric field, $\mathbf{h}$ is the magnetic field, $\mathbf{b}$ is the magnetic flux density, and $\mathbf{j}_e$ is the source term. By applying a Fourier transform, these expressions can be rewritten in the frequency domain as

$$\nabla \times \mathbf{E} + i\omega\mu\mathbf{H} = 0, \tag{3}$$

$$\nabla \times \mathbf{H} - \sigma\mathbf{E} = \mathbf{J}_e, \tag{4}$$

where $\mathbf{E}$, $\mathbf{H}$, and $\mathbf{J}_e$ are the Fourier transforms of the time-domain fields. In the frequency domain, the fields and fluxes are related by the constitutive relations $\mathbf{J} = \sigma\mathbf{E}$ and $\mathbf{B} = \mu\mathbf{H}$, where the electrical conductivity σ relates the current density $\mathbf{J}$ and the electric field. The magnetic permeability μ relates the magnetic field to the magnetic flux density $\mathbf{B}$. For the work here, we assume that the earth's magnetic permeability is constant, so $\mu = \mu_0$, where μ_0 is the permeability of free space. The electrical resistivity is $\rho = 1/\sigma$: Both terms are used throughout this paper. The frequency-domain expressions use the angular frequency $\omega = 2\pi f$ (f is the frequency in Hz).

There are multiple variations and survey arrangements for EM methods. Galvanic sources use grounded current electrodes, which can be at the surface or in boreholes. Inductive sources consist of wire loops that are ungrounded. Transmitter loops at the surface can have sides ranging from meters to hundreds of meters, while coils can be used as borehole transmitters (Wilt et al., 1995).

The transmitter currents can be sinusoidal, and this leads to a frequency-domain survey. Each frequency samples the earth differently in accordance with its skin depth. The skin depth d (in m) is the distance that a plane wave propagates in a homogeneous background before attenuating by a factor of $1/e$:

$$d \approx 500\sqrt{\rho/f}, \tag{5}$$

where ρ (in Ωm) is the background resistivity and f (in Hz) is the frequency. Thus, each frequency is sensitive to earth structure at different distances from a transmitter. Data from a frequency-domain EM survey are complex numbers written as an amplitude and phase or as in-phase and
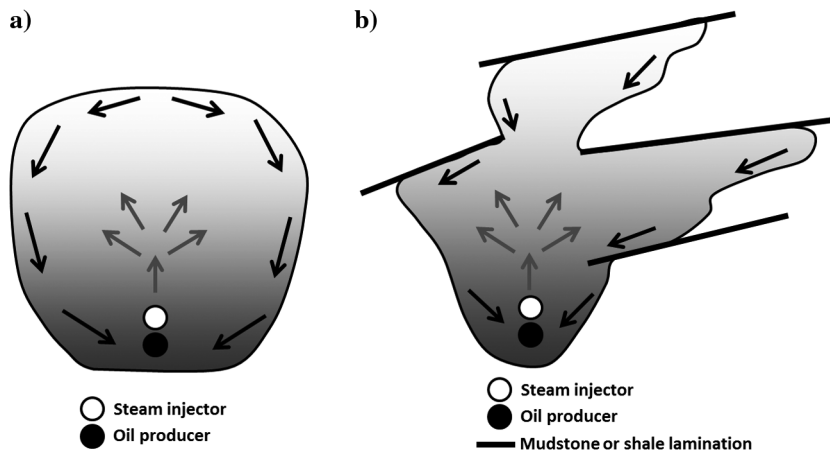

Figure 1. (a) A theoretical balloon-shaped SAGD steam chamber and (b) a more realistic, irregular chamber. The steam chamber can be affected by heterogeneity within the reservoir, causing an irregular shape. Modified from Peacock (2010).

quadrature. DC resistivity is a special case of frequency-domain EM that uses a single frequency, $f = 0$, and galvanic sources. The regions of illumination are governed purely by geometry and the electrical conductivity.

Time-domain EM experiments are carried out by using a different waveform, such as a step-off current, and data are generally measured in the "off-time." The time-varying magnetic field produced by the step-off current diffuses into the earth according to

$$r \approx 1260\sqrt{t\rho}, \tag{6}$$

where r (in m) is the diffusion distance and t (in s) is the time since transmitter shut-off. Data are real numbers measured at multiple logarithmically spaced time channels (TC). Frequency- and time-domain data are related through Fourier transforms, and the general concept that data at high frequencies and early TC sample the earth closer to the transmitter, whereas low-frequency and late time data sample the earth farther from the transmitter.

Receivers can measure a variety of EM fields. The magnetic flux $\mathbf{B}$ and its time-derivative $\partial \mathbf{B}/\partial t$ are measured with a magnetometer and a coil, respectively. Depending on the system, noise floors for $\partial \mathbf{B}/\partial t$ can range from 10^{-9} to 10^{-11} V/m^2 for a transmitter with a moment of 1 Am^2. A SQUID sensor provides the highest precision for a $\mathbf{B}$-field sensor: approximately 20 femtotesla or 2×10^{-5} nT. Electric field sensors are grounded or capacitive electrodes, which measure a potential difference. When the distance between the two sensors is small, the potential difference is divided by the distance between the sensors to yield an estimate of the electric field $\mathbf{E}$. Otherwise, the potential difference itself is used as a datum. This is the case for DC resistivity surveys. Capacitive sensors have low-noise thresholds and can measure fields as small as 10^{-11} V/m with dipole lengths of 20–40 m (Hibbs et al., 2014). Table 1 summarizes the noise thresholds. Fields may be measured at the surface or in a borehole. The magnitude of the measured fields can be boosted by increasing the transmitter moment, either by increasing the amount of current, the area of the loop, and/or by the number of turns in the loop. Receiver effective areas can also be increased by adding extra turns of wire in the receiver.

All EM methods are sensitive to electrical conductivity, but the choice of which survey to use depends upon the sought geophysical parameters, geologic context, acquisition efficiency, noise issues, desired resolution, and cost. Survey design is thus complicated. One can always get better images by using more transmitters, having more data, and putting sources and receivers closer to the target. To make some practical progress with investigating realistic and cost effective surveys, we take the following approach. We restrict transmitters and receivers to be on the surface or in boreholes that are likely to exist because they are required for other measurements. Even with these restrictions, there are numerous geometries and combinations that can be used. We select some of these, simulate the data, and carry out 3D inversions. The efficacy of our survey is evaluated by the detail that is observed in our inverted model. In carrying out the inversions, we are careful to ensure that any floor value for assigned uncertainty is at least as large as the noise floors provided in Table 1. It is well-known that the inverse problem is nonunique and that the model recovered from an inversion depends upon the details of the inversion algorithm itself. For this reason, we outline some important details of our inversion methodology. All inversions carried out in this paper follow the same methodology although different numerical codes are implemented.

Inversion methodology

The inverse problem is posed as an optimization problem that incorporates Tikhonov and Arsenin (1977) regularization. To solve the problem numerically, Maxwell's equations, shown in equations 3 and 4, are discretized. The earth is represented as a set of prismatic cells, each of which has a constant conductivity (Haber et al., 2004). Letting $\mathcal{F}$ denote the Maxwell operator, the forward problem is written as

$$\mathcal{F}[\mathbf{m}] = \mathbf{d}, \tag{7}$$

where the model $\mathbf{m}$ contains the conductivity values of the cells. The data $\mathbf{d}$ consist of $\mathbf{E}$, $\mathbf{H}$, and/or $\partial \mathbf{B}/\partial t$, in frequency or in time, in the three spatial directions (x, y, and z). We invert the data by minimizing the objective function:

$$\phi(\mathbf{m}) = \phi_d + \beta\phi_m(\mathbf{m}), \tag{8}$$

where ϕ_d is the misfit between the observed data and the predicted data:

$$\phi_d = \|\mathbf{W}_d(\mathcal{F}[\mathbf{m}] - \mathbf{d}^{\mathrm{obs}})\|_2^2. \tag{9}$$

The matrix $\mathbf{W}_d$ contains the reciprocal uncertainty values assigned to each datum. The goal is to find a model that fits the data to within the uncertainty but also has certain features, i.e., similarity to a reference model $\mathbf{m}_{\mathrm{ref}}$, minimal structure, particular geologic features, and/or a priori information. This is included using a model objective function $\phi_m(\mathbf{m})$

$$\phi_m(\mathbf{m}) = \alpha_s \|\mathbf{W}_s(\mathbf{m} - \mathbf{m}_{\mathrm{ref}})\|_2^2 + \sum_{i=1}^{3} \alpha_i \|\mathbf{W}_i(\mathbf{m} - \mathbf{m}_{\mathrm{ref}})\|_2^2, \tag{10}$$

where the first term controls how close the model is to the reference model, and the last term dictates smoothness in the three spatial directions (x, y, z) denoted by $i = 1, 2, 3$. The α values regulate the relative importance of each term, whereas the $\mathbf{W}$ matrices can incorporate additional weighting and a priori information. In addition, we have the flexibility to only allow certain cells to change value. Including the reference model $\mathbf{m}_{\mathrm{ref}}$ in the smoothness terms allows changes in the model to be smooth while preserving certain characteristics, but it can be removed to allow for a smoother overall model. A trade-off parameter β balances the data misfit and the

Table 1. When inverting data, uncertainties are assigned as a percentage of the data plus a noise floor. We assign the noise floor either as a value based on instrument sensitivities, of which representative minimum values are given, or a value such that a percentage of the data fall below the noise floor.

Data type	Instrument sensitivity
V	1×10^{-6} V
E	1×10^{-12} V/m
B	2×10^{-5} nT
$\frac{\partial B}{\partial t}$	1×10^{-11} V/m^2

model objective function. Standard Gauss-Newton methodologies are used to solve the inverse problem (Oldenburg and Li, 2005; Nocedal and Wright, 2006).

Several inversion codes are used in this paper. Oldenburg and Li (1994) describe the 2D inversion of DC resistivity, whereas the 3D algorithm is presented in Haber et al. (2012). Frequency-domain data were inverted on either a 3D tensor or octree mesh (Haber et al., 2004), whereas the time-domain data were inverted using the algorithm described in Oldenburg et al. (2013). For simulating and inverting data, we need to design a synthetic model. The first step is to develop a background model that has representative structures and conductivities.

Geology

The Athabasca oil sands can be found at the surface to depths as large as 400 m (Hinkle and Batzle, 2006). Although the lithology is complex, we simplify it into a few distinct layers: an overburden, a shale cap rock, the oil sands reservoir, and a limestone basement unit (Hein and Cotterill, 2006). The overburden is Quaternary in age and consists primarily of glacial tills. Below the Quaternary lies the Mannville Group, which includes the cap rock and oil sands reservoir. The Grand Rapids and Clearwater Formations consist of shales, which act as the cap rock for the oil reservoir. The Wabiskaw Member, part of the Clearwater Formation, is a transgressional layer above the McMurray Formation. In the Athabasca oil sands, the McMurray Formation is the main oil sands reservoir and consists of unconsolidated sands with heavy oil, or bitumen. Below the McMurray lies a Devonian limestone unit, which is generally resistive. However, due to the presence of dissolved Prairie Evaporites, the resistivity of the Devonian unit can sometimes be low. The McMurray Formation and Quaternary are generally more resistive than the conductive cap rock. General thicknesses and resistivity values for each unit are presented in Table 2.

Change in conductivity

Empirical formulations can provide reasonable resistivity estimations. Archie's law is often used to determine the resistivity of clean sands:

$$\frac{1}{\rho} = \sigma = \frac{\phi^m s^n \sigma_w}{\tau}, \qquad (11)$$

where ρ is the resistivity, σ is the conductivity, ϕ is the porosity, m is the cementation exponent, s is the water saturation, n is the saturation exponent, σ_w is the water conductivity, and τ is the tortuosity.

Table 2. General thicknesses and resistivity values for lithology units within the Athabasca oil sands (Bauman, 2005; Zhdanov et al., 2013).

Geologic unit	Formation name	Thickness (m)	Resistivity (Ωm)
Overburden	Quaternary	0–200	100 s
Cap rock	Grand Rapid and Clearwater	0–30	2–30
Oil sands	McMurray	50–100	100–1000
Limestone	Devonian	–	1–1000

This expression, however, does not adequately represent the resistivity of oil-rich sands and does not accurately account for changes in resistivity due to steaming (Mansure et al., 1993). Other expressions, such as the Waxman-Smits equation, incorporate more parameters, such as the behavior of clays, and can approximate the resistivity better than Archie's law. The Waxman and Smits (1968) equation is written as follows (Mansure et al., 1993):

$$\sigma = \frac{s^n \left(\sigma_w + \frac{BQ_v}{s} \right)}{F^*}, \qquad (12)$$

where B is the specific counterion conductance and Q_v is the cation exchange capacity. The water conductivity $\sigma_w = c(T + 21.5)$ is dependent on salinity c and temperature T. The shaley-sand formation factor F^* is expressed as

$$F^* = \frac{\tau}{\phi^m} \left(1 + \frac{BQ_v}{\sigma_w} \right). \qquad (13)$$

The specific counterion conductance B is expressed as

$$B = 3.83(0.04T)(1 - 0.83 \exp(-0.5\sigma_w|_{T=25})), \qquad (14)$$

and the cation exchange capacity is written as

$$Q_v = \frac{V_{cl}C\delta}{\phi}, \qquad (15)$$

where V_{cl} is the percentage of clay, C is the cation exchange coefficient, and δ is the density. Previous studies (e.g., Mansure et al., 1993; Tøndel et al., 2014) show that the resistivity of an oil-bearing reservoir will decrease when steamed. The amount of change will depend on the changes in the parameters in equation 12, but primarily on temperature, salinity, and water saturation.

FEASIBILITY STUDY OF EM METHODS

We start the feasibility study by generating a small irregular steam chamber from a 4D seismic time-delay attribute map, which acts as a first-order representation of steam thickness. The attribute map is translated into height (Figure 2), and a subset is used as the steam chamber. The pyramid-shaped anomalous steam chamber (Figure 3a) varies in thickness from 5 to 50 m. It extends 150 m in the easting direction and 200 m in the northing direction and lies between 200 and 250 m below the surface. Based on published values of resistivity decreases (Mansure et al., 1993; Tøndel et al., 2014), we choose a value of 10 Ωm for the steam chamber, which is hosted in a uniform 400 Ωm background. This conductivity model allows us to understand the inherent challenges of survey design and detectability. Its simplicity also promotes fast turnaround times for forward modeling and inversion.

An important component of the geologic model is the Clearwater Formation that acts as a cap to the oil-bearing McMurray Formation. This conductive layer channels currents from grounded sources and acts as a shield to the sought steam chamber. The layer also acts as an attenuator for any surface inductive source. We add the Clearwater Formation to the initial chamber model. The layer

has a thickness of 50 m and a resistivity of 17 Ωm. The model in Figure 3b shows the cap rock overlying the irregular steam chamber.

The model in Figure 3b is discretized into cubic cells and different transmitters and receivers are selected and input into the numerical forward modeling. Our interest is in detecting the existence and details of the steam chamber in the presence of the background geology. This requires two forward modelings: one with the chamber and one with just the background geology. We define two metrics that can be used to estimate the feasibility of an EM survey to detect the steam chamber: relative and absolute difference anomalies. The relative difference (RD) addresses whether the secondary field (or the response due to the steam chamber) is large enough compared with the total field:

$$\text{RD} = \left| \frac{F^S}{F^T} \right| * 100, \tag{16}$$

where F^T is the total field (electric or magnetic) and F^S is the secondary field: $F^S = F^T - F^P$, where F^P is the primary field associated with a conductivity model that does not contain the sought anomaly. The absolute difference (AD) addresses the magnitude of the secondary field:

$$\text{AD} = |F^S|. \tag{17}$$

It should be larger than the sensitivity of the receiver and larger than various sources of noise (e.g., EM noise and geologic noise). The absolute difference can be increased by changing some elements of the survey, such as increasing the magnitude of the transmitter current. However, this will not affect the relative difference, which is dependent on the geology and the transmitter-target coupling.

We image the synthetic irregular chamber using these transmitters: (1) borehole galvanic sources, (2) borehole magnetic sources, and (3) large inductive sources at the surface. For each survey, data are forward modeled using a current of 1 A in the transmitter and the median RD and AD are calculated for each data type (e.g., the imaginary component of $\mathbf{E}_z$). We then take the average of these values for each field (e.g., the magnetic field), and these are shown in Table 3. We add 2% Gaussian noise to each forward-modeled data set. Uncertainties are assigned as a percentage of the data plus a noise floor. The noise floor can be either (1) a value based on instrument sensitivity or (2) a value such that 10% of the data fall below the noise floor, depending on which is higher. This is done so that the noise floor is not unreasonably low and hopefully reflects what might be achievable in practice. Table 1 lists the instrument sensitivities used for the different measurements. In each 3D inversion, the initial and reference model is the true background model shown in Figure 3b, and for the 2D inversions, a 2D section through this model was used. The final misfit for each inversion was at, or close to, the target misfit.

Galvanic sources

The conductive cap rock is a major impediment to using grounded sources at the surface.

Numerical experiments showed that too much of the current is channeled into the cap rock or attenuated as it attempts to propagate through. We therefore consider surveys that implement galvanic sources in boreholes.

Based on current industry practices, we begin with DC resistivity, using a crosswell survey, which has been used to monitor SAGD steam chambers in two dimensions (Tøndel et al., 2014). Our design consists of a crosswell survey using four boreholes, spaced 200 and 300 m apart, that straddle the location of the steam chamber (Figure 4a). These locations would be typical for observation wells for SAGD operations (e.g., Zhang et al., 2007). Electrodes are placed along the borehole every 20 m, for a total of 80 electrodes. This survey provides 98 transmitters with 40 voltage measurements for each transmitter, for a total of 3920 measurements. The data in the 200 m spaced boreholes have a larger RD and AD than those in the 300 m spaced boreholes ("Crosswell 200" and "Crosswell 300" in Table 3). This indicates that the data are sensitive to the synthetic
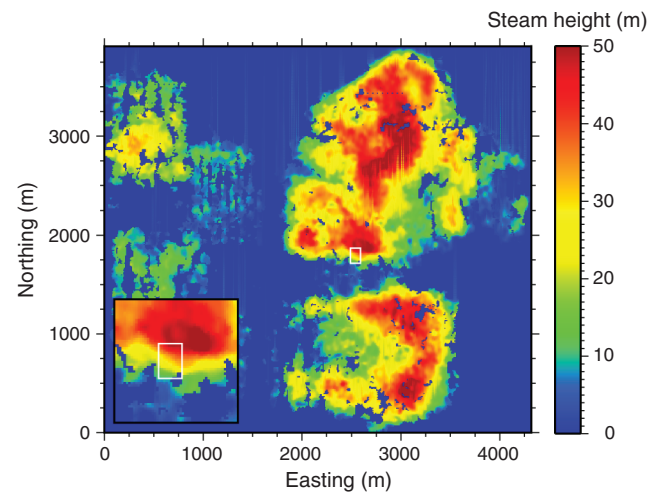

Figure 2. Seismic time-delay attribute data from multiple SAGD well pads were translated into steam chamber height. A small subset, represented by the white rectangle, is used to generate the synthetic irregular steam chamber.
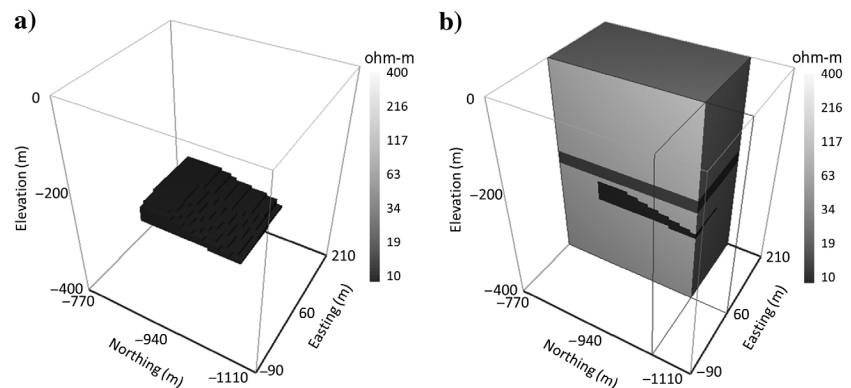

Figure 3. (a) A synthetic steam chamber with a pyramidal shape reflects the irregular growth that can occur in SAGD. The chamber has a resistivity of 10 Ωm and is hosted in a 400 Ωm background. (b) A cap rock with thickness of 50 m and a resistivity of 17 Ωm is added above the steam chamber. There is a 10 m gap between the top of the steam chamber and the bottom of the cap rock.

steam chamber, but we note that closer proximity to the target allows for greater detectability.

Each crosswell data set is inverted separately using a 2D inversion algorithm (Oldenburg and Li, 1994). The final models are shown in (Figure 5b). The models have substantial artifacts, especially for the survey where the boreholes are 300 m apart. For the example with a well spacing of 200 m, the anomaly is recovered, but the resistivity is too high and the shape is not well defined. Given that the steam chamber has a 3D shape, it is difficult to fit a 2D model to these data. We therefore invert the two 3D data sets simultaneously (Haber et al., 2012). The recovered model shows a smooth, compact body with no artifacts (Figure 5c). However, the steam chamber shape is poorly defined, and the resistivity is much higher than the true value.

By designing a 3D survey, we can achieve the same level of resolution but with fewer transmitters and data. Our design approach uses anomalous secondary currents of a confined body to select transmitters that will excite the steam chamber in multiple directions and generate substantial secondary fields (Devriese and Oldenburg, 2014). The redesigned survey has 24 bi-pole transmitters and 124 borehole receivers per transmitter, which are distributed in six boreholes (Figure 4b). The electrodes are placed every 20 m down the hole, providing 2976 voltage measurements. This is 25% fewer data than the crosswell survey. Although the AD values are lower for this survey compared with the crosswell survey, the RD values are substantially higher ("Crosswell 3D" in Table 3). The recovered model is shown in Figure 5d. The resolution of the steam chamber is very similar to the example using the crosswell survey, although the resistivity is slightly lower. This shows that by developing a more ap-

propriate survey design that collects 3D information about the target, we can achieve similar results using fewer data compared with a more standard survey design.

The model in Figure 5d still does not provide enough information to confidently identify the anomaly as either a regular or irregular steam chamber. Part of the difficulty is that the inversions are allowing all cells in the 3D volume to vary. We can improve upon the result if we fix the background and allow only the cells within the bitumen layer to change. The background model could come from a combination of geophysical surveys and well logs. We note that the survey design used here to find the steam is not an adequate survey from which to estimate the entire background model.

For the following inversions, we assume that the background, including the low-resistivity cap rock, is known. In the inversion, only the resistivity of cells within the 60 m thick bitumen layer is allowed to change. The recovered model (Figure 5e) has significantly improved, especially in the value of recovered resistivity, which now reaches a low of 10 Ωm. Nevertheless, we still cannot confidently interpret the anomaly as an irregular steam chamber. These examples show that although the data are able to detect the steam chamber with DC sources, there is not enough information to recover a model with the desired resolution. Therefore, we turn our investigation toward EM methods.

Multifrequency galvanic sources

By measuring data at multiple frequencies, more information can be obtained about the subsurface using the same survey design as in the previous section. We chose seven frequencies, ranging from 1 to 10 kHz based on skin depth (equation 5) and analyzing the changes in amplitude and phase of the secondary currents in a confined conductor. The survey geometry remains the same as in the DC resistivity experiment (Figure 4b) except that the transmitters now operate at seven frequencies. To model these data, we require solving the full Maxwell's equations, for which we use a finite-volume technique (Haber et al., 2004). The data include electric and magnetic fields. The RD and AD metrics, shown in Table 3 as "Galvanic EM," indicate that the steam is detectable.

The data are inverted in three dimensions with resistivity changes restricted to cells within the bitumen layer. The recovered model (Figure 5f) is far superior to any of the inversions that only use DC resistivity data. The irregularity of the steam chamber is imaged: It becomes progressively thinner toward the southwest, and the depth to the top of the steam increases. Moreover, the chamber manifests itself as a substantial conductor with resistivity values as low as 2 Ωm. This contrasts with the muted dynamic range of the resistivity recovered in Figure 5c and 5e. Overall, we conclude that by using EM data at multiple frequencies and designing a 3D survey, we obtain important information about the steam chamber's existence and location.

Table 3. For each survey, the RD and AD values are calculated for each data type (e.g., the imaginary component of E_z) at each receiver location using equations 16 and 17. These are then used to calculate a median value for each data type. Last, the median values are subsequently averaged to get a global RD or AD for the voltage, electric field, or magnetic field. For the time domain, the median RD and AD values for the magnetic flux density are provided for the early, middle, and late TCs.

DC resistivity surveys

Survey	RD:V	AD:V
Crosswell 200	10.3	0.0054
Crosswell 300	4.5	0.0049
Crosswell 3D	13.3	0.0037

Frequency-domain surveys

Survey	RD:E, H	AD:E, H
Galvanic EM	19, 19	1.3×10^{-5}, 4.0×10^{-6}
Borehole coils	47, 9	2.1×10^{-10}, 8.6×10^{-11}
Surface loop — surface RX	0.28, 0.19	9.6×10^{-8}, 3.9×10^{-8}
Surface loop — borehole RX	38, 5	2.5×10^{-7}, 1.0×10^{-7}

Time-domain surface loop survey — borehole RX

	RD:$\partial B/\partial t(x, y, z)$	AD:$\partial B/\partial t(x, y, z)$
Time channel $4-30$ μs	0.21, 0.70, 0.63	1.2×10^{-9}, 3.4×10^{-10}, 5.6×10^{-10}
Time channel $60-600$ μs	1.34, 7.21, 1.77	2.4×10^{-9}, 8.2×10^{-10}, 1.9×10^{-9}
Time channel $900-6000$ μs	2.98, 10.11, 3.84	3.1×10^{-10}, 9.7×10^{-11}, 2.6×10^{-10}

Inductive sources

Two forms of inductive sources are of practical significance. The first is a borehole magnetic source, which is made up of multiple turns of a current wire. The strength of the source depends upon the area of the coil, the number of turns in the wire, and the current. The magnetic moment of these sources can vary from 1000 to 10,000 Am^2 (Wilt et al., 1995). The other source is a large loop that lies on the surface. Such a source is appealing because the logistics of deploying a surface transmitter are straightforward and anything done on the surface is generally less expensive than downhole surveys. The drawback is that a surface transmitter is physically distant from the target, and hence, the primary field is attenuated by geometry, causing inductive losses before it has an opportunity to excite the target. In the case of the Athabasca oil sands, which are only a few hundred meters deep, this deficit might be overcome.

Small borehole transmitters

We keep the same six boreholes used in the previous example and use our survey design approach to delineate locations for 29 vertical magnetic dipole transmitters (Figure 4c). Electric and magnetic fields are forward modeled using the same seven frequencies as before and a magnetic dipole moment of 1 Am^2. The 125 receivers are distributed among the six boreholes in the same locations as in the previous example. The RD values indicate that the steam chamber is detectable, but the AD values are much lower than those seen in the galvanic examples ("Borehole coils" in Table 3). These values are boosted by assuming a much larger dipole moment. The data are inverted in three dimensions, and the recovered model is shown in Figure 5g. The model nicely recovers the essential shape and resistivity of the steam chamber to the same extent as the galvanic example. However, there are subtle differences, which are attributed to the different types of transmitters.
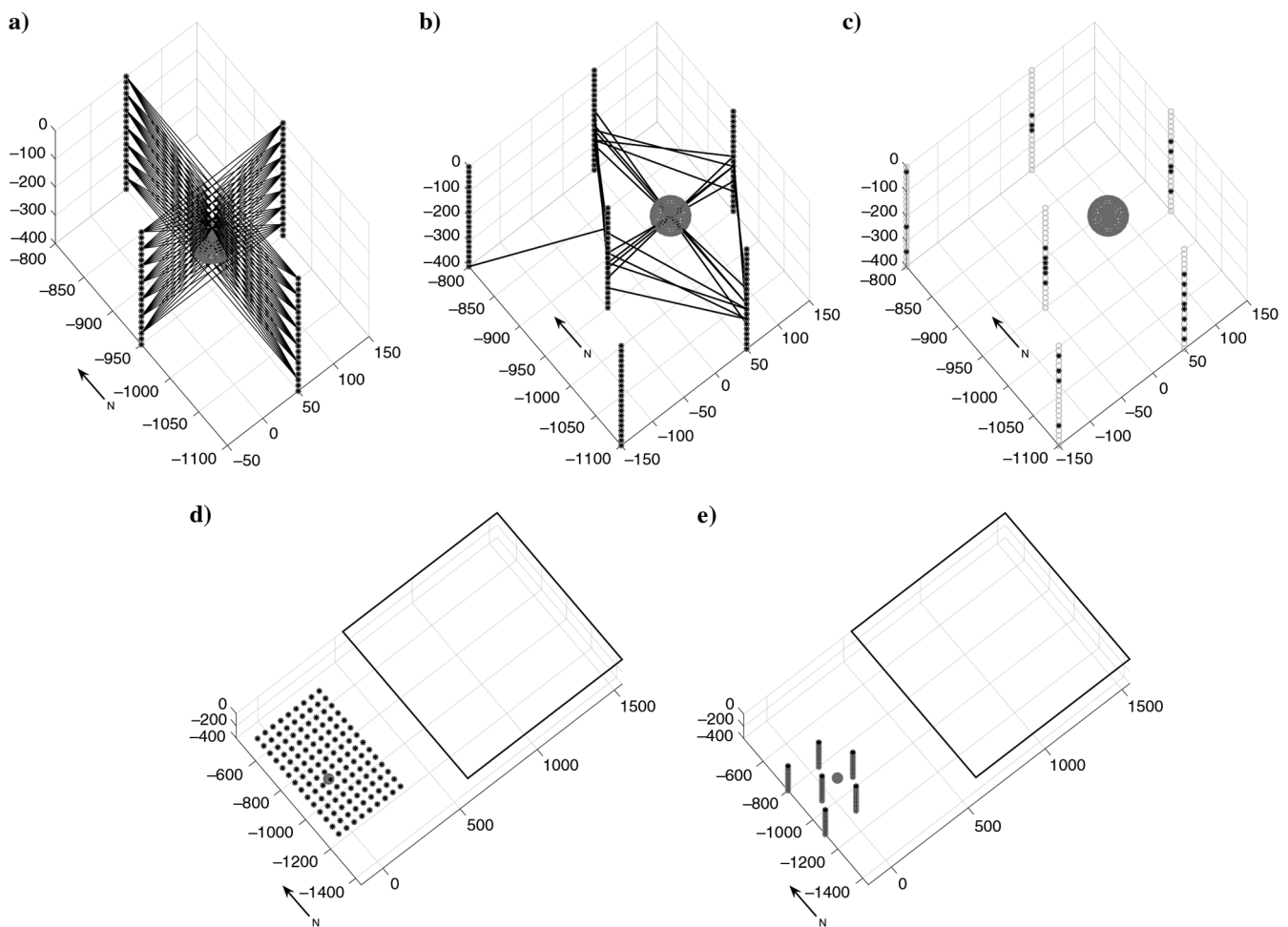

Figure 4. Various electric and EM surveys were tested in the feasibility study: (a) Two traditional crosswell surveys straddle the area of interest. The survey has 98 current electrode pairs and 40 voltage measurements per current electrode pair. (b) This galvanic survey was designed to excite the anomaly in three dimensions. The survey has 24 current electrode pairs and 124 receivers per current electrode pair. Electrode locations are shown as black stars. The lines connect the current electrodes. In (c), black dots show the locations of the magnetic dipole sources, whereas gray dots indicate the receiver locations. In (d and e), black lines indicate the transmitter loop. Receivers are indicated using black dots. In each figure, the location of the irregular steam chamber is shown using a gray sphere.
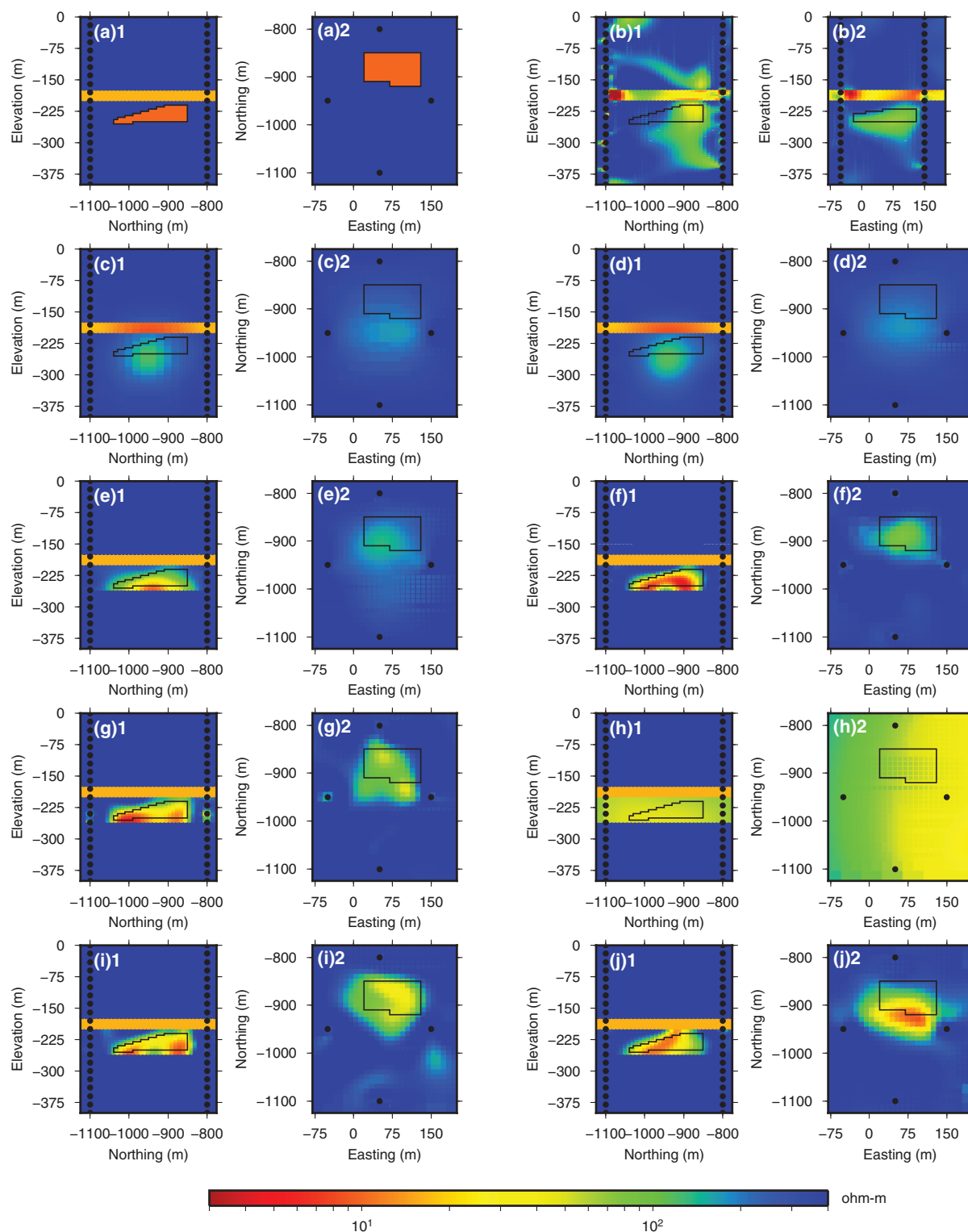
Figure 5. Each panel, except (b), shows a cross section at 50 m easting and a depth slice at −215 m elevation, shown as 1 and 2, respectively. (a) True model. (b) Two 2D recovered models using the DC surveys in Figure 4a. Panel (b1) is at 50 m easting and panel (b2) is at −950 northing. (c) Three-dimensional recovered model using the combined DC survey in Figure 4a. (d) Three-dimensional recovered model using the DC survey in Figure 4b. In (e-j), conductivity changes are restricted to the bitumen layer between elevations of −200 and −260 m: (e) 3D recovered model using the DC survey in Figure 4b, (f) 3D recovered model using the EM survey in Figure 4b, (g) 3D recovered model using the survey in Figure 4c, (h) 3D recovered model using the survey in Figure 4d, (i) 3D recovered model using the frequency-domain survey in Figure 4e, and (j) 3D recovered model using the time-domain survey in Figure 4e.

Large surface transmitter: Frequency domain

An ideal cost-effective survey would undoubtedly have transmitters and receiver combinations located at the surface. Again, multiple transmitter configurations are possible to explore, but one of the more likely candidates is a large-loop transmitter because this can provide a high magnetic moment. Here, we choose a transmitter that is 1×1 km with a current of 1 A. Surface receivers are placed in a grid with 50 m spacing, for a total of 126 receivers (Figure 4d). Five components ($\mathbf{E}_x$, $\mathbf{E}_y$, $\mathbf{H}_x$, $\mathbf{H}_y$, and $\mathbf{H}_z$) are forward modeled in the frequency domain using the same seven frequencies used before, which range from 1 Hz to 10 kHz. The RD values, shown in Table 3 as "Surface loop — surface RX," indicate that the survey is not very sensitive to the steam chamber. This was confirmed by inverting the data: The recovered model (Figure 5h) is unable to recover the steam chamber.

This result is significantly improved by using borehole receivers (Figure 4e). Receivers are placed at the same locations in the six boreholes as in previous examples. Electric and magnetic fields are forward modeled at the same seven frequencies. The RD and AD values are much higher when using borehole receivers (Table 3 as "Surface loop — borehole RX"), indicating that the steam chamber is more likely to be detected.

The 3D inversion shown in Figure 5i is able to nicely recover the steam chamber. In fact, this image is similar, but not identical, to the other EM inversions, where the shape and the resistivity of the irregular steam chamber are imaged.

Large surface transmitter: Time domain

As a compliment to the frequency-domain experiments considered thus far, we also explore the use of time-domain EM. A major difference between time-domain and frequency-domain surveys is that we generally measure time-domain responses after the current in the transmitter has been shut off. This means that measurements only include the secondary response, whereas frequency-domain measurements include the primary and secondary responses.

We repeat the survey using the surface transmitter and borehole receivers. The data correspond to the time-derivative of the magnetic field using a step-off waveform (Oldenburg et al., 2013). Data are measured at 11 off-time TC, which were chosen using equation 6: 4, 6, 9, 30, 60, 90, 300, 600, 900, 3000, and 6000 μs. The RD values vary for different TC, with low values for early times and higher values at middle and late times (Table 3). The AD values are highest for the early TC. These metrics indicate that the steam chamber is being detected and that the measured TC capture the majority of the response of the anomaly. The data are inverted in three dimensions, which yields the recovered model presented in Figure 5j. The result is similar to the frequency-domain inversion with good recovery of the shape and resistivity of the irregular steam chamber.

Summary

We examined the feasibility of electric and EM methods using an irregularly shaped steam chamber. Based on current industry practices, we first used a DC resistivity survey and showed that 3D inversions are essential to reduce artifacts that can arise if data are inverted in two dimensions. By using a survey with fewer data, but designed to detect a 3D object, we were able to gain somewhat

better information than traditional crosswell surveys. Nonetheless, the recovered model still lacked resolution in shape and resistivity amplitude.

The major impact of the feasibility study was to illustrate the large benefit of carrying out multifrequency or time-domain EM surveys. In all cases, the combination of borehole receivers with an EM transmitter provided data that were highly sensitive to the steam chamber, and the inversions recovered models with superior resolution in shape and better recovery of the resistivity amplitude. Using EM methods, it became feasible to distinguish the steam chamber as growing irregularly. Of special significance was the result obtained from using a surface transmitter and borehole receivers. The receivers for this survey would be similar to those used in crosswell surveys, and can thus be installed permanently in the wells. The transmitter would be a large wire loop at the surface, which is generally inexpensive to deploy. Because of the utility and cost effectiveness of this survey, we apply it to an example based on an existing field site in the following section.

SYNTHETIC STUDY FOR A FIELD SITE

The feasibility results in the first part of this paper show that EM methods can be superior to ERT surveys in recovery of SAGD steam chambers. We also note that costs can be decreased by using surface methods, but that borehole receivers are necessary to measure the secondary response. In the SAGD environment, not all receiver types may withstand the high heat, but it has been shown that electrodes can be used for long periods of time (Tøndel et al., 2014). Therefore, we now use a surface loop transmitter with borehole electrode receivers that measure only the vertical component of the electric field. This survey is used to image three SAGD steam chambers in a layered medium that was constructed from well-logs and physical properties from an actual field site.

Site background

The Aspen property is owned by Imperial Oil, and it is the future site of several SAGD well pads. The project area lies approximately 45 km northeast of Fort McMurray and 25 km southeast of Fort MacKay in northeastern Alberta, Canada. Numerous vertical wells have been drilled on and around the Aspen property (Kennedy, 2013). Because many of these are publicly available, we use eight vertical wells that contain resistivity logging and lithology picks (Wynne et al., 1994).

1D model

We first compile the resistivity logging data from the eight wells. Horizons were added for the tops of the overlying Quaternary units, the Grand Rapids Formation, the Clearwater Formation (including the Wabiskaw Member), the McMurray Formation, and the underlying Devonian units (Wynne et al., 1994; Kennedy, 2013). Figure 6 shows the lithology picks, stratigraphic column, and resistivity log data. For each lithologic unit, the resistivity logging data are averaged to generate a semisynthetic 1D resistivity model for the Aspen property. The 1D model is overlain on the resistivity logging data in Figure 6c.

At the Aspen property, the oil saturation is approximately 80% for the McMurray Formation with an average porosity of 33% (Kennedy, 2013). Density is reported as 2.65 g/cm^3, the cementation exponent

m as 1.8, and the saturation exponent n as 1.7. The background temperature at the Aspen property is 7°C. We used a tortuosity value of 1.63 (Bell et al., 2011).
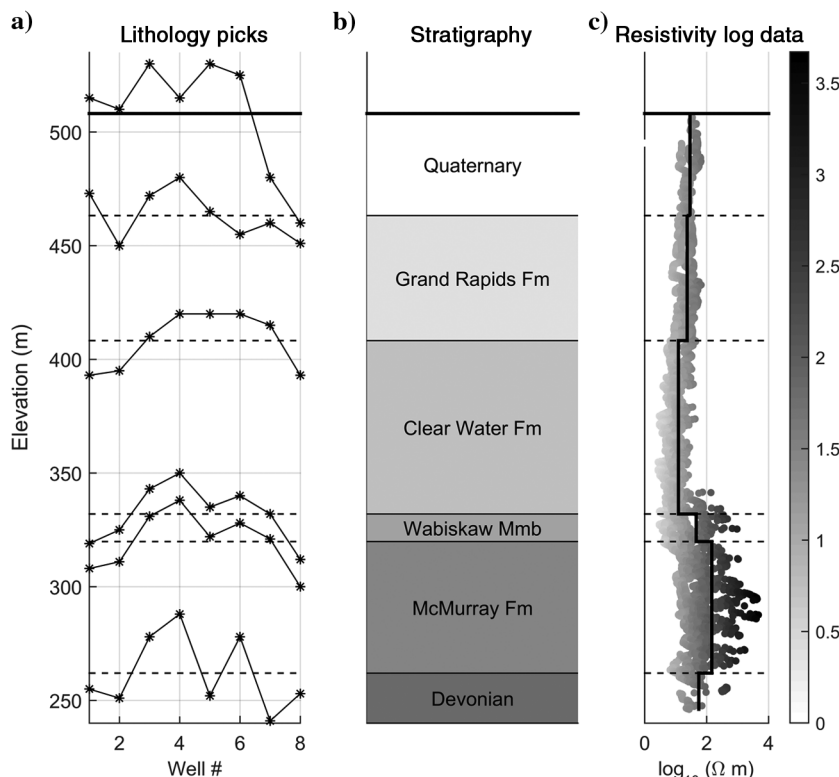

Figure 6. For each of the eight wells, (a) the top of each lithology unit was picked and (b) their elevations were averaged to generate a single stratigraphic column. (c) The resistivity logs from the eight wells are plotted with the average resistivity for each lithology unit.
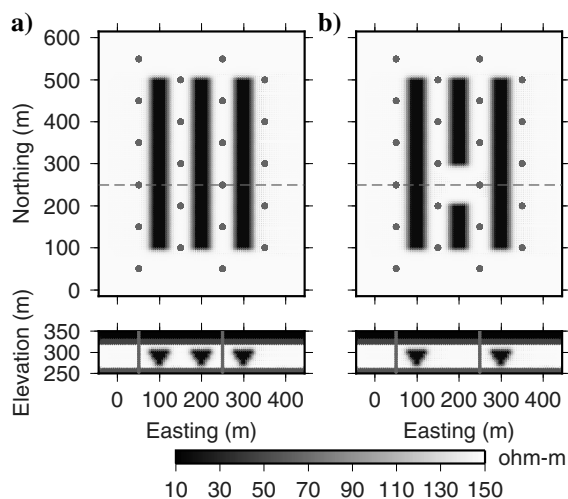

Figure 7. (a) True model showing three steam chambers. (b) True model showing three chambers, where the center chamber is impeded due to a blockage. Each panel shows a depth slice 215 m below the surface and a cross section of the reservoir at a northing of 250 m. In plan view, gray dots denote borehole locations and the gray line indicates the location of the cross section. The borehole locations in the cross section are indicated using gray dots.

We assumed a clay volume of 1% and a cation exchange capacity of 0.25 meq/g for the McMurray Formation, whereas 60% and 0.4 meq/g, respectively, for the Wabiskaw Member (S. Charles, personal communication, 2012). Salinities were estimated as 2460 and 530 ppm for the McMurray Formation and Wabiskaw Member (Kennedy, 2013). Applying these parameters in equations 12–15, we calculate a resistivity of 147 Ωm for the McMurray Formation and 46 Ωm for the Wabiskaw Member. These values match with those from the resistivity well logs.

Modeling steam chambers

We adapt the formulation by Reis (1992) to generate a series of steam chambers:

$$W_s = tH\sqrt{2/a}, \qquad (18)$$

where W_s is the half-width of the steam chamber, H is the vertical distance between the top of the steam chamber and the producing well, $a = 0.4$ is a dimensionless temperature coefficient, and $t = 0.25$ is a dimensionless time since production started. This example uses three chambers with a height of 35 m. Each chamber is 400 m in length and is separated by 100 m at the base.

For this investigation, salinity and saturation are kept constant over time. The temperature will radiate outward from the steam chamber and thus alter the conductivity of the surrounding geology. We use the temperature distribution described by Reis (1992) and formulate it as a function of radial distance d from the steam chamber:

$$T(d) = T_0 + (T_s - T_0)e^{-\frac{aUd}{\alpha}}, \qquad (19)$$

where T_0 is the initial reservoir temperature, T_s is the steam temperature, U is the steam front velocity, and α is the temperature diffusivity. The constant $a = 0.4$ is the same as in equation 18. For this problem, the temperature diffusivity is 0.0507 m²/day, the steam front velocity is 0.0417 m/day, and the steam temperature is 200°C.

Given the initial resistivity values (Figure 6), we now calculate the resultant resistivity due to the change in temperature using equations 12–15. Instead of a constant initial temperature, the 3D temperature distribution calculated in equation 19 is used. The calculated resistivity within the steam chambers is 16 Ωm, which then diffuses back to the background value away from the chambers. The 3D resistivity model is shown in Figure 7a. Because heterogeneity can cause steam chambers to not grow properly, we add a blockage to the middle steam chamber, impeding the steam growth. The blockage is 100 m long and is surrounded by 50 m of steam to the south and 250 m of steam to the north. Figure 7b shows the perturbed steam chamber resistivity model.

STEAM CHAMBER IMAGING USING SURFACE LOOP TRANSMITTERS

We have shown that it is possible to excite a steam chamber with a large surface loop carrying harmonic waveforms at different frequencies. Here, we make use of two transmitters: one to the east of the chambers and the other to the north. Each transmitter is 1×1 km (Figure 8). Because of the geometry, the EM fields couple differently with the steam chambers, and hence, the two surveys provide complementary information.

We investigate the models in Figure 7a and 7b for three scenarios: (1) using the eastern transmitter, (2) using the northern transmitter, and (3) using both transmitters. We restrict the receiver locations to observation wells that would be routinely drilled. Figure 8 shows the locations of the 22 wells in relation to the transmitters and steam chambers. Although in principle, all components of the electric and magnetic fields can be measured in the boreholes, here we restrict the data to a single type: the vertical component of the electric field. Receivers are spaced every 20 m in the observation wells, except in the bitumen reservoir where there are receivers at every 5 m. Three frequencies (10, 50, and 100 Hz) were chosen based on skin depth (equation 5) and the average resistivity of the layers above the McMurray Formation.

For each model and each survey, the z-component of the electric field is forward modeled at each frequency and 2% Gaussian noise is added to the data. Uncertainties are assigned as a percentage of the data, and a noise floor before the data are inverted in three dimensions using the code described in Haber et al. (2012). For each inversion, the background 1D model was used as the initial and reference model. Resistivity changes are limited to the heavy oil reservoir between elevations of 263 and 318 m. Because the steam is expected to decrease the resistivity, the resistivities in the recovered model were limited to be no higher than 147 Ωm, which was the assumed resistivity of the McMurray Formation. Because the orientations of the horizontal well pairs are known, we increase model smoothness in that direction by increasing α_y in equation 10. For each inversion, the following parameters are used: $\alpha_s = 1e - 5$, $\alpha_x = \alpha_z = 1$, and $\alpha_y = 10$.

Example with nonperturbed chambers

We first consider the model shown in Figure 7a. For each transmitter, we calculate the RD and AD values using equations 16 and 17. Table 4 presents the median values. These metrics show that the steam chambers are much more detectable using the eastern transmitter compared with the northern transmitter. This is attributed to different coupling between the transmitter and steam chambers. When the primary electric field is parallel to the main axis of the steam chambers (as when using the eastern transmitter), there are major currents in the north–south direction. That is, there is good coupling with the steam chambers. For the northern transmitter, the primary electric fields are in the east–west direction and currents are forced through a succession of resistive and conductive regions.

To quantify this, we calculate the secondary current density for these two survey designs

(Devriese et al., 2014), where the anomalous conductivity consists of the three steam chambers. For the eastern transmitter, the anomalous currents are substantial and point predominantly in the northern direction; whereas for the northern transmitter, the currents point in the eastern direction. Figure 9a and 9d shows the secondary current density for the eastern and northern transmitters, indicating that the excitations from the two surveys are perpendicular and that the excitation is greater closer to the respective transmitter. We also note
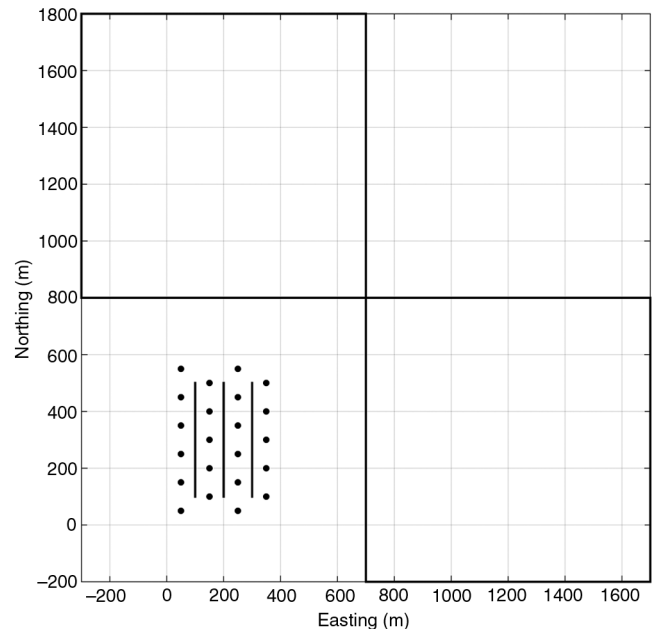

Figure 8. Two surface transmitters, each 1×1 km, at the surface are used individually and simultaneously to recover three SAGD steam chambers. For each survey, the z-component of the electric field is measured at receivers in boreholes (dots) that surround the three horizontal wells (black lines). Each borehole has 33 receivers, spaced every 20 m. Receivers are spaced every 5 m in the bitumen reservoir.

Table 4. For each survey, the median RD and AD values are calculated for the z-component of the electric field. These metrics show that the eastern transmitter is more sensitive to the steam chambers and the nonsteamed blockage.

Nonperturbed steam chambers — Compared with 1D model		
Survey	RD	AD
East TX	72	4.5×10^{-8}
North TX	45	2.4×10^{-8}

Perturbed steam chambers				
	Compared with 1D model		Compared with nonperturbed model	
Survey	RD	AD	RD	AD
East TX	76	4.8×10^{-8}	8	6.1×10^{-9}
North TX	51	3.3×10^{-8}	1.6	1.1×10^{-9}

that the current density due to the eastern transmitter is larger than currents due to the northern transmitter. This shows that the amount of excitation differs but that complementary information is being provided by the two transmitters. From this, we expect that the eastern transmitter will provide a better inversion result than the northern transmitter; whereas, a simultaneous inversion of both will yield the best result.

These analyses are supported by the inversions of the data. Plan view and cross sections of the 3D recovered models for the eastern and northern transmitters are shown in Figure 10b and 10c. The first major observation is that the overall location of the steam chambers is well-imaged horizontally. More detailed scrutiny shows that the inversion model from the eastern transmitter suggests that there are two major north–south conductors. The eastern-most conductor is colocated with the eastern steam chamber, but the other conductor is a blurred image of the central and western chambers. Its maximum value lies midway between the two chambers, close to the observation wells. This blurring is a consequence of the transmitter being on the eastern side. The primary currents from the transmitter are weakened on the west side, compared with the east, because they are farther from the transmitter and some shielding arises from the eastern-most chamber. A second transmitter on the west would help to overcome this difficulty. So too would a transmitter located at the northern or southern end of the steam zones. We choose the northern transmitter as a second transmitter because it excites the steam chambers from a different direction. The northern transmitter generates a weaker conductivity anomaly, but it has better delineation of the three chambers. The conductivity highs, al-

though somewhat subtle, are colocated with the steam chambers. Figure 10b and 10c shows the cross sections for recovered conductivity. Rather good horizontal resolution is observed, but there is little vertical resolution.

A simultaneous inversion of data from both transmitters is shown in Figure 10d. The image is considerably enhanced compared with either of the individual inversions. The three chambers are now high-amplitude structures located in their correct horizontal location. These inversion results show that excitation in the steam chambers highly depends on the location of the transmitter and that anomalous currents and metrics about data differences can be used to predict the sensitivity to the steam chambers before inversion. We note that these images were generated with only minimal a priori information, restricting the steam chambers to be preferentially oriented in the north-south direction. Additional known information, such as fixing the conductivity around the observation wells or incorporation of sensitivity weighting to push the recovered model away from the observation locations, was not included. Doing so provided results with enhanced resolution, but our goal here is to generate a model that is controlled as much as possible by the EM data and relies only minimally upon a priori information.

Example with a perturbed chamber

During SAGD processes, a steam chamber may not grow as expected due to reservoir heterogeneity, which blocks the steam from penetrating through the reservoir. We thus consider the example where the middle chamber has such a blockage (Figure 7b). For

Figure 9. The top and bottom rows show the secondary currents for the eastern and northern transmitters, respectively. Panels (a and d) show the secondary currents between the background 1D model and the unperturbed model (Figure 7a). Panels (b and e) show the currents between the background 1D model and the perturbed model (Figure 7b). Panels (c and f) show the secondary currents in the blockage using the perturbed and unperturbed 3D models.
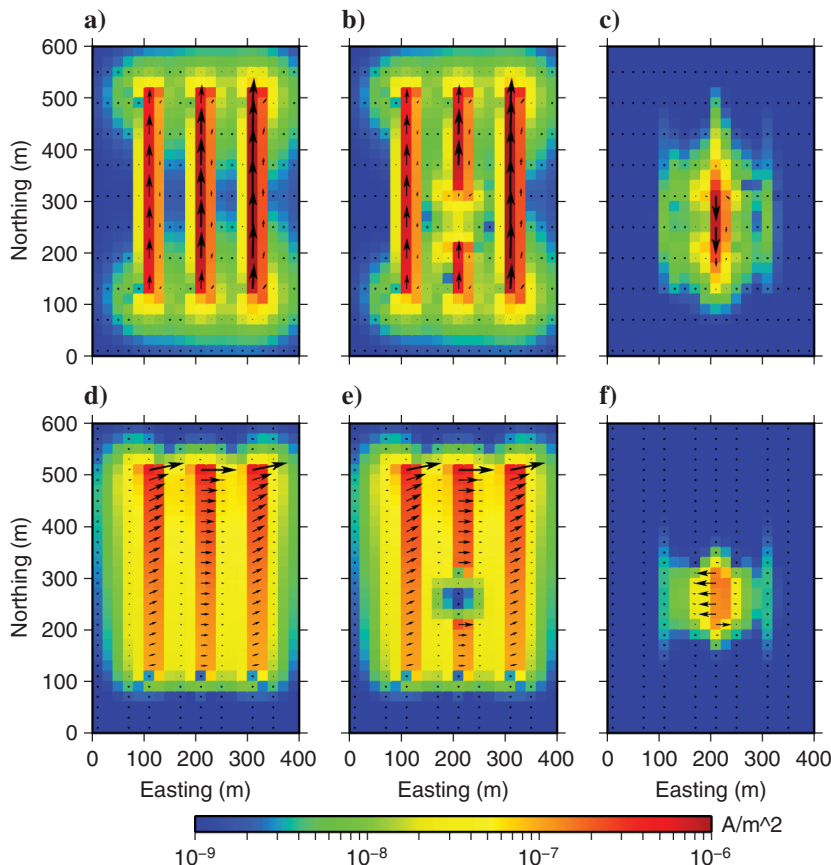
each transmitter, median RD and AD values are calculated to evaluate the potential effectiveness of the surveys. The results are tabulated in Table 4. We first compare the metrics using the earth containing the perturbed steam chamber and the 1D background. Those results are comparable to, but slightly larger than, the metrics for the previous inversion where we looked for continuous steam chambers. We next evaluate the RD and AD assuming the background model is the continuous steam chamber embedded in a 1D background, and the model of interest is the same conductivity with a blockage. The metrics are considerably reduced but the values are large enough for us to infer that the two steam chamber models, one with and one without the perturbation, should be distinguishable from the data. For both transmitters, we also calculate the secondary current density for the blockage compared with the 1D background model (Figure 9b and 9e) and the unperturbed model (Figure 9c and 9f). This again indicates that the two transmitters provide complementary information about the subsurface.

The data for the two transmitters are inverted individually, and the results are shown in Figure 11b and 11c. The blocked region is visible in both. The results from the eastern transmitter contain some of the features shown in Figure 10b corresponding to an un-

Figure 11. (a) True model showing three steam chambers, where the center chamber is impeded due to a blockage. Recovered models using (b) the eastern transmitter, (c) the northern transmitter, and (d) both transmitters. Each panel shows a depth slice 215 m below the surface and a cross section of the reservoir at a northing of 250 m. In plan view, white dots denote borehole locations and the white line indicates the location of the cross section. The borehole locations in the cross section are indicated using white dots.

blocked chamber. At the northern end, the high conductivity is mislocated over one of the observation wells; that is, it is between the two steam chambers. Nevertheless, the location and recovered conductivity of the blocked region are very well recovered. The image from the northern transmitter displays many of the characteristics in Figure 10c, but it too clearly shows the blocked area.

The results are further improved by simultaneously inverting data from both surveys. Figure 11d shows better resolution and recovered resistivity of the three steam chambers with improved imaging of the blockage. Again, there is little vertical resolution, but the high conductivities fan out toward the top of the reservoir as they do in the true model.

CONCLUSION

We have shown the feasibility of using EM methods to detect and image SAGD steam chambers in the Athabasca oil sands. Our research shows that better results can be obtained by using multifrequency or time-domain EM methods than by using traditional DC resistivity in a crosswell setting. Furthermore, the results show that
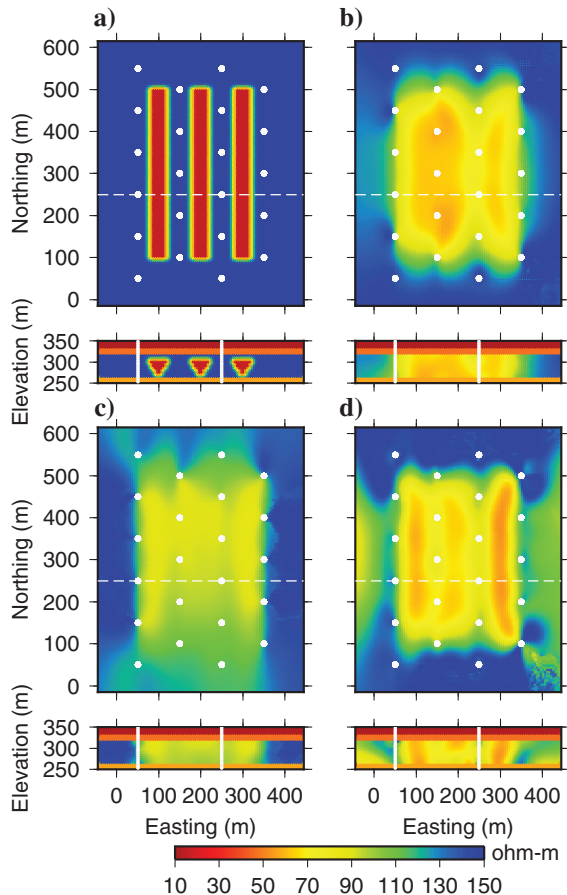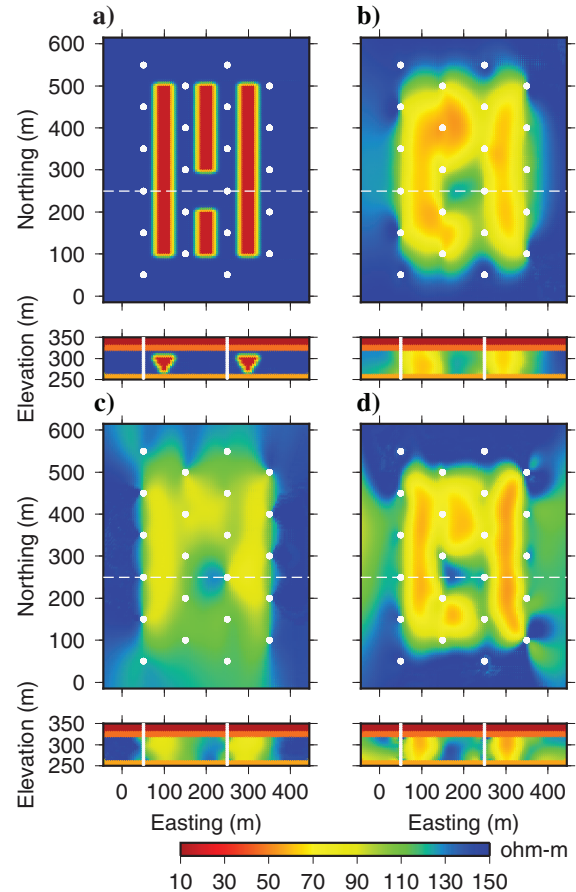

Figure 10. (a) True model showing three regular SAGD steam chambers. Recovered models using (b) the eastern transmitter, (c) the northern transmitter, and (d) both transmitters. Each panel shows a depth slice 215 m below the surface and a cross section of the reservoir at a northing of 250 m. In plan view, white dots denote borehole locations and the white line indicates the location of the cross section. The borehole locations in the cross section are indicated using white dots.

the combination of a surface transmitter and borehole receivers yields models that can identify irregularly shaped steam chambers and areas with no steam growth. These images can be valuable for oil production throughout the SAGD process.

We applied a survey using large surface loop transmitters and borehole receivers to a synthetic example based on a site in the Athabasca oil sands. The data were limited to the vertical component of the electric field, which can be measured by electrodes within observation wells. The benefit of this configuration is that the electrodes can withstand the high-temperature SAGD environment, and the loop transmitters are easily deployed at the surface. We examined the use of two transmitter configurations which were chosen because they generated orthogonal excitation within the reservoirs.

Although each survey provided valuable information about the conductivity, models from an individual survey are prone to artifacts. We have shown that inverting data from two transmitters substantially reduces these artifacts and produces an enhanced resolution image. We note that these transmitters provided perpendicular excitation of the target and that additional strategically placed transmitters could further improve recovery of the chambers. For this study, we were able to discern the location and extent of the no-growth area with two transmitters. However, the vertical resolution of conductivity in the bitumen layer was fairly poor using this configuration. Further development of the survey design could improve this.

Furthermore, the availability of a priori information can greatly enhance the final result. In these examples, limiting resistivity changes to the reservoir layer, and providing directional smoothing, based on the orientation of the horizontal wells, helped the inversion to provide better images. This type of information would be available during SAGD operations and can therefore be easily incorporated when inverting field data. One downside of these constraints is that the focus is on the reservoir layer and any other changes occurring (such as changes in the cap rock) will not be adequately imaged. Additional improvement can be obtained by working with more detailed background models, constraining the conductivity of the model around the observation locations, and adding other a priori information that might be available. In our example, we limited the amount of constraints applied to the inversion to focus on the ability of the EM data to recover the steam chambers.

Surveys as those used here can readily be used to monitor the SAGD steam chamber growth over time and at greater frequency than typical surface seismic surveys. As EM methods are further researched to understand how they can be used to monitor SAGD processes it will become important to consider the infrastructure at the surface and within the reservoir. The cased injector and producer wells will generate an EM signal, and further research is required to understand their impact on detecting the steam chamber. Also, infrastructure noise will need to be contended with. Some of these issues can be handled through time-lapse inversion techniques. In addition, time-lapse inversion techniques can be used to invert multiple EM data sets over time, providing several interpretations per year and thus, better oversight of the SAGD process.

Overall, the ability to permanently install transmitters and receivers means data can be collected often and remotely. Combined with efficient inversion techniques and a priori information, these EM methods allow for fast turn-around and practically real-time results. This can greatly impact monitoring capabilities when combined with less-frequently collected seismic surveys for better management and planning of SAGD production in the Athabasca oil sands.

REFERENCES

Al-Bahlani, A.-M., and T. Babadagli, 2009, SAGD laboratory experimental and numerical simulation studies: A review of current status and future issues: Journal of Petroleum Science and Engineering, **68**, 135–150, doi: 10.1016/j.petrol.2009.06.011.

Bauman, P., 2005, 2-D resistivity surveying for hydrocarbons – A primer: CSEG Recorder, **30**, 25–33.

Bell, J., A. Boateng, O. Olawale, and D. Roberts, 2011, The influence of fabric arrangement on oil sand samples from the estuarine depositional environment of the upper McMurray Formation: Presented at the AAPG International Conference and Exhibition.

Butler, D. B., and R. J. Knight, 1998, Electrical conductivity of steam-flooded clay-bearing geologic materials: Geophysics, **63**, 1137–1149, doi: 10.1190/1.1444414.

Butler, R. M., 1994, Steam-assisted gravity drainage: Concept, development, performance and future: Journal of Canadian Petroleum Technology, **33**, 44–50, doi: 10.2118/94-02-05.

Dembicki, E. A., 2001, The challenges in delineating Suncor's firebag in-situ oil sands project: Presented at the Canadian Society of Petroleum Geologists Rock the Foundation Convention.

Devriese, S. G. R., and D. W. Oldenburg, 2014, Enhanced imaging of SAGD steam chambers using broadband electromagnetic surveying: 84th Annual International Meeting, SEG, Expanded Abstracts, 765–769.

Devriese, S. G. R., D. W. Oldenburg, and S. Charles, 2014, Using electromagnetic methods to image SAGD steam chambers: Presented at the 2014 CSEP CSPG CWLS Geoconvention Conference.

Engelmark, F., 2007, Time-lapse monitoring of steam assisted gravity drainage (SAGD) of heavy oil using multi-transient electro-magnetics (MTEM): Presented at the 2007 CSPG CSEG Convention.

Engelmark, F., 2010, Heavy oils: Reservoir characterization and production monitoring: SEG, 301–308.

Ferguson, J. F., F. J. Klopping, T. Chen, J. E. Seibert, J. L. Hare, and J. L. Brady, 2008, The 4D microgravity method for waterflood surveillance: Part 3 – 4D microgravity surveys at Prudhoe Bay, Alaska: Geophysics, **73**, no. 6, WA163–WA171, doi: 10.1190/1.2992510.

Forgues, E., J. Meunier, F. Gresillon, C. Hubans, and D. Druesne, 2006, Continuous high-resolution seismic monitoring of SAGD: 76th Annual International Meeting, SEG, Expanded Abstracts, 3165–3169.

Haber, E., U. M. Ascher, and D. W. Oldenburg, 2004, Inversion of 3D electromagnetic data in frequency and time domain using an inexact all-at-once approach: Geophysics, **69**, 1216–1228, doi: 10.1190/1.1801938.

Haber, E., J. Granek, D. Marchant, E. Holtham, D. Oldenburg, and R. Shekhtman, 2012, 3D inversion of DC/IP data using adaptive OcTree meshes: 82nd Annual International Meeting, SEG, Expanded Abstracts, doi: 10.1190/segam2012-1438.1.

Hein, F. J., and D. K. Cotterill, 2006, The Athabasca oil sands — A regional geological perspective, Fort McMurray Area, Alberta, Canada: Natural Resources Research, **15**, 85–102, doi: 10.1007/s11053-006-9015-4.

Hibbs, A. D., T. R. Petrov, J. Pendleton, A. Agundes, S. Kouba, T. Hall, D. Boyle, T. Martin, C. Schenkel, and H. F. Morrison, 2014, Advances in electromagnetic survey instrumentation and the use of a cased borehole for imaging a deep formation: Presented at the EAGE 76th Annual International Conference and Exhibition.

Hinkle, A., and M. Batzle, 2006, Heavy oils: A worldwide overview: The Leading Edge, **25**, 742–749, doi: 10.1190/1.2210073.

Kennedy, A., 2013, Application for approval of the Aspen Project: Technical Report, Imperial Oil Resources Ventures Limited, 1–42.

Krawchuk, P., M. A. Beshry, G. A. Brown, and B. Brough, 2006, Predicting the flow distribution of total E&P Canada's Joslyn Project horizontal SAGD producing wells using permanently installed fiber-optic monitoring: Presented at the SPE Annual Technical Conference and Exhibition.

LaBrecque, D. J., A. L. Ramirez, W. D. Daily, A. M. Binley, and S. A. Schima, 1996, ERT monitoring of environmental remediation processes: Measurement Science and Technology, **7**, 375–383, doi: 10.1088/0957-0233/7/3/019.

Mansure, A. J., R. F. Meldau, and H. V. Weyland, 1993, Field examples of electrical resistivity changes during steamflooding: SPE Formation Evaluation, **8**, 57–64, doi: 10.2118/20539-PA.

Marion, B., M. Safdar, M. Wilt, P. Zhang, F. Loh, and A. Nalonnil, 2011, Crosswell technologies: New solutions for enhanced reservoir surveillance: Presented at the SPE Enhanced Oil Recovery Conference.

Nocedal, J., and S. Wright, 2006, Numerical optimization: Springer.

Oldenborger, G. A., M. D. Knoll, P. S. Routh, and D. J. LaBrecque, 2007, Time-lapse ERT monitoring of an injection/withdrawal experiment in a shallow unconfined aquifer: Geophysics, **72**, no. 4, F177–F187, doi: 10 .1190/1.2734365.

Oldenburg, D. W., E. Haber, and R. Shekhtman, 2013, Three dimensional inversion of multisource time domain electromagnetic data: Geophysics, **78**, no. 1, E47–E57, doi: 10.1190/geo2012-0131.1.

Oldenburg, D. W., and Y. Li, 1994, Inversion of induced polarization data: Geophysics, **59**, 1327–1341, doi: 10.1190/1.1443692.

Oldenburg, D. W., and Y. Li, 2005, Near-surface geophysics: SEG, 59–150.

Peacock, M. J., 2010, Athabasca oil sands: Reservoir characterization and its impact on thermal and mining opportunities: Petroleum Geology Conference Series, **7**, 1141–1150.

Ramirez, A., W. Daily, D. LaBrecque, E. Owen, and D. Chesnut, 1993, Monitoring an underground steam injection process using electrical resistance tomography: Water Resources Research, **29**, 73–87, doi: 10.1029/92WR01608.

Ranganayaki, R. P., A. E. Akturk, and S. M. Fryer, 1992, Formation resistivity variation due to steam flooding: A log study: Geophysics, **57**, 488–494, doi: 10.1190/1.1443264.

Reis, J. C., 1992, A steam-assisted gravity drainage model for tar sands: Linear geometry: Journal of Canadian Petroleum Technology, **31**, 14–20, doi: 10.2118/92-10-01.

Reitz, A., R. Krahenbuhl, and Y. Li, 2015, Feasibility of time-lapse gravity and gravity gradiometry monitoring for steam-assisted gravity drainage reservoirs: Geophysics, **80**, no. 2, WA99–WA110, doi: 10.1190/geo2014-0217.1.

Singhai, A. K., and C. C. Card, 1988, Monitoring of steam simulation in McMurray Formation, Athabasca Deposition, Alberta: Journal of Petroleum Technology, **40**, 483–490, doi: 10.2118/14215-PA.

Strobl, R., B. Jablonski, and M. Fustic, 2013, Opportunities and challenges in accessing stranded pay and heterogenous reservoirs in SAGD bitumen projects: Presented at the GeoConvention 2013 — Integration.

Tikhonov, A., and V. Y. Arsenin, 1977, Methods for solving ill-posed problems: John Wiley and Sons Inc.

Tøndel, R., H. Schütt, S. Dümmong, A. Ducrocq, R. Godfrey, D. LaBrecque, L. Nutt, A. Campbell, and R. Rufino, 2014, Reservoir monitoring of steam-assisted gravity drainage using borehole measurements: Geophysical Prospecting, **62**, 760–778, doi: 10.1111/gpr.2014.62.issue-4.

Waxman, M. H., and L. J. M. Smits, 1968, Electrical conductivities in oil-bearing shaly sands: SPE Journal, **8**, 107–122, doi: 10.2118/1863-A.

Wilt, M. J., D. L. Alumbaugh, H. F. Morrison, A. Becker, K. H. Lee, and M. Deszcz-Pan, 1995, Crosswell electromagnetic tomography: System design considerations and field results: Geophysics, **60**, 871–885, doi: 10 .1190/1.1443823.

Wolf, K., T. Vanorio, and G. Mavko, 2008, Measuring and monitoring heavy-oil reservoir properties: The Leading Edge, **27**, 1138–1147, doi: 10.1190/1.2978976.

Wynne, D. A., M. Attalla, T. Berezniuk, M. Brulotte, D. K. Cotterill, R. Strobl, and D. Wightman, 1994, Athabasca Oil Sands Data McMurray/Wabiskaw Oil Sands Deposit — Electronic Data: Technical report, Alberta Geologic Survey, http://ags.aer.ca/publications/SPE_006.html, accessed 5 April 2016.

Zhang, W., S. Youn, and Q. Doan, 2007, Understanding reservoir architectures and steam-chamber growth at Christina Lake, Alberta, by using 4-D seismic and crosswell seismic imaging: SPE Reservoir Evaluation and Engineering, **10**, 446–452, doi: 10.2118/97808-PA.

Zhdanov, M. S., L. Cox, and J. Rudd, 2013, Paradigm change in 3D inversion of airborne EM surveys: Case study for oil sands exploration near Fort McMurray, Alberta: First Break, **31**, 81–85.